Chapter 5
Multi-spacecraft Current Estimates at Swarm

Malcolm Wray Dunlop, J.-Y. Yang, Y.-Y. Yang, Hermann Lühr and J.-B. Cao

Abstract In this chapter the application of the curlometer technique to various regions of the inner magnetosphere and upper ionosphere and for special circumstances of sampling is described. The basic technique is first outlined, together with the caveats of use, covering: the four-spacecraft technique, its quality factor and limitations; the lessons learnt from Cluster data, together with issues of implementation, scale size and stationarity, and description of the key regions covered by related methodology. Secondly, the application to the Earth's ring current region is outlined, covering: the application of Cluster crossings to survey the ring current; the use of the MRA (magnetic rotation analysis) method for field curvature analysis; the use of THEMIS (Time History of Events and Macroscale Interactions during Sub-storms mission) three-spacecraft configurations to sample the ring current, and future use of MMS (Magnetospheric MultiScale mission) and Swarm data, i.e. the case of small separations. Thirdly, the application of the technique to the low altitude regions covered by Swarm is outlined, covering: the extension of the method to stationary signals; the use of special configurations and adjacent times to achieve 2, 3, 4, 5 point analysis; the use of the extended 'curlometer' with Swarm close configurations to compute 3-D current density, and a brief indication of the computation of current sheet orientation implied by 2-spacecraft correlations. Fourthly, the direct coordination of Cluster and Swarm to check the scaling and coherence of field-aligned currents (FACs) is outlined.

M. W. Dunlop (✉) · J.-Y. Yang · J.-B. Cao
School of Space and Environment, Beihang University, Beijing 100191, P.R. China
e-mail: malcolm.dunlop@stfc.ac.uk; m.w.dunlop@rl.ac.uk

M. W. Dunlop
RAL Space, Rutherford Appleton Laboratory, STFC-UKRI, Chilton, UK

Y.-Y. Yang
The Institute of Crustal Dynamics, CEA, Beijing 100085, P.R. China

H. Lühr
GFZ, Telegrafenberg, 14473 Potsdam, Germany

5.1 Introduction

In this chapter, we discuss the performance and lessons learnt from the application of the multi-spacecraft curlometer technique to the regions of the upper ionosphere and inner magnetosphere and discuss the adaptability of the method to situations where full spatial coverage cannot be achieved. Firstly, we review the method and secondly we consider its use both in situ in the ring current and in regions covered by field-aligned currents. The standard method used to interpret the Swarm dual-spacecraft data is discussed in detail in Chap. 6.

5.2 Basic Application of the Curlometer

Although fundamentally, currents in plasmas are set up by the differential motion of charged particles, in practice this approach requires that the whole particle 3D particle velocity distribution is measured for all ion species and electrons, where the currents are derived from computation of the bulk moments from the distribution functions. These measurements often rely on spacecraft spin (and thus have limited time resolution), or arrays of detectors, to obtain the full distribution. Recent results from the Magnetospheric Multiscale (MMS) mission (Burch et al. 2016), covering primarily the outer magnetosphere, however, benefit from distributions measured at high-time resolution, in addition to multi-point sampling at small (several km) spatial distances. Nevertheless, previous space missions have suffered from low cadence or incomplete particle measurements (examples of previous use of particle moments can be found in Henderson et al. 2008; Petrukovich 2015). In fact, the generation of currents in highly conducting space plasmas produce magnetic fields that modify the existing magnetic field (e.g. the Earth's internal magnetic field). As a result of quasi-neutrality, for highly conducting plasmas the displacement current, $\mu_0\epsilon_0\partial\mathbf{E}/\partial t$, where $\mathbf{E}$ is the electric field, can be neglected in Maxwell's equations Russell et al. 2016) so that the magnetic field generated by currents can be given by Ampère's law:

$$\mu_0\mathbf{J} = \mathbf{curl}(B)$$

where $\mathbf{J}$ is the current density and $\mathbf{B}$ the magnetic field. This relation enables us to derive the strength and orientation of currents directly from the magnetic field and its gradients, but requires measurements at multiple spatial positions, simultaneously. Magnetic fields in space can typically be measured with higher accuracy and higher time resolution than particle moments. Multiple spacecraft flying in formation, and each measuring the magnetic field, allow a linear estimate of Ampère's law (above) to be made, i.e. the electric current density from $\mathbf{curl}(B)$. The method, termed the curlometer technique (Dunlop et al. 1988), was introduced to utilize four-point measurements in space (the minimum to return a vector estimate of current density); anticipating the four-spacecraft Cluster mission (Escoubet et al. 2001). Although
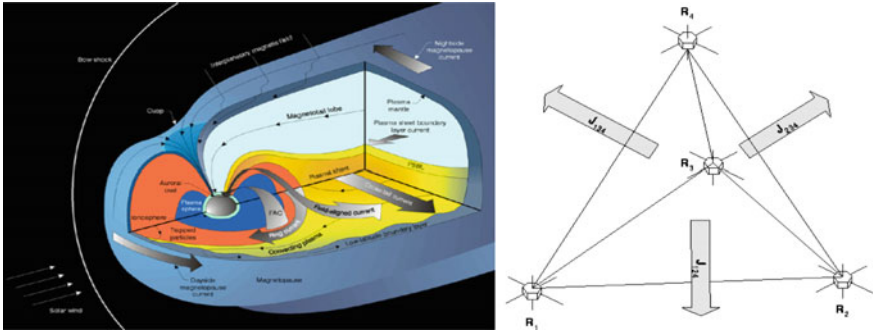
Fig. 5.1 Depiction of the large-scale currents in the Earth's magnetosphere (adapted from Kivelson and Russell (1995), left) and the curlometer concept (after Dunlop et al. 1988, right)

robust and reliable in many regions of the magnetosphere (such as the magnetopause, the magnetotail and the ring current), the accuracy of the method is limited by uncertainties in the spacecraft separation distances, timing and the form (scale size) of the current structure; as well as accuracy of the magnetic field measurements (see Fig. 5.1).

5.2.1 Four-Spacecraft Technique: Quality Factor and Limitations

The curlometer method estimates the average current density within the tetrahedral configuration formed by the individual spacecraft positions and measured magnetic fields, based on the assumption that: $\mathbf{curl}(\boldsymbol{B}) = \mu_0\boldsymbol{J}$. The basic method provides all components of the electric current density by either estimating linear approximations to the spatial gradients needed for $\mathbf{curl}(\boldsymbol{B})$, or by using the linear (discrete), integral form of Ampère's law ($\mu_0 \int \boldsymbol{J}.\mathrm{d}\mathbf{s} = \int B.\mathrm{d}l$). The latter provides an estimate of the average current density, J_{1ij}, normal to the face 1ij of the tetrahedron (see the right hand side of Fig. 5.1) from:

$$\mu_0 < \boldsymbol{J} > .(\Delta\boldsymbol{R}_i \wedge \Delta\boldsymbol{R}_j) = \Delta\boldsymbol{B}_i.\Delta\boldsymbol{R}_j - \Delta\boldsymbol{B}_j.\Delta\boldsymbol{R}_i, \tag{5.1}$$

e.g. $\mu_0<\boldsymbol{J}>_{123}.(\Delta\boldsymbol{r}_{12}\,\hat{}\,\Delta\boldsymbol{R}_{13}) = \Delta\boldsymbol{B}_{12}.\Delta\boldsymbol{R}_{13} - \Delta\boldsymbol{B}_{13}.\Delta\boldsymbol{R}_{12}$ (division of the magnitude $\mu_0\Delta\boldsymbol{r}_{12}\,\hat{}\,\Delta\boldsymbol{R}_{13}$ gives J explicitly).

Here, $\Delta\boldsymbol{B}_{1i}$, $\Delta\boldsymbol{R}_{1i}$ (which are the differences in the measured magnetic field and positions from spacecraft 1 to each of the others) have been shortened in notation to $\Delta\boldsymbol{B}_i$, $\Delta\boldsymbol{R}_i$, which represent the vector difference in the measured magnetic field vector and spatial position vector. Any reference spacecraft can be used and of course each of the four faces of the tetrahedron gives an estimate of the current density normal to that face and in principle can be used independently. Three faces of the tetrahedron

combine to provide three non-coplanar components of the current (which can then be used to construct the average vector current density in any system of coordinates), while the fourth is redundant (see below).

The average value of div$B$ over the volume of the tetrahedron can also be estimated from $< div(B) > \left| \Delta \boldsymbol{R}_i . \Delta \boldsymbol{R}_j \wedge \Delta \boldsymbol{R}_k \right| = \left| \sum_{cyclic} \Delta \boldsymbol{B}_i . \Delta \boldsymbol{R}_j \wedge \boldsymbol{R}_k \right|$,

e.g. $<div(\boldsymbol{B})>_{1234}(\Delta \boldsymbol{R}_{12} \cdot \Delta \boldsymbol{R}_{13} \wedge \Delta \boldsymbol{R}_{14}) = \Delta \boldsymbol{B}_{12} \cdot \Delta \boldsymbol{R}_{13} \wedge \Delta \boldsymbol{R}_{14} + \Delta \boldsymbol{B}_{13} \cdot \Delta \boldsymbol{R}_{14} \wedge \Delta \boldsymbol{R}_{12} + \Delta \boldsymbol{B}_{14} \cdot \Delta \boldsymbol{R}_{12} \wedge \Delta \boldsymbol{R}_{13}$,

Here, any non-zero value indicates the approximate size of the neglected non-linear gradients (Dunlop et al. 2002, 2016, 2018; Robert et al. 1998 and see also Haaland et al. 2004), indirectly (since div$B$ = 0 exactly). The relative orientation and spatial scale of the current structures sampled, compared with the shape and size of the spacecraft configuration ultimately control the error in the linear estimates through the neglected non-linear gradients in B. This error is unknown in absolute terms, but usually can be indirectly monitored through the quality parameter, Q = |div$B$|/|**curl**(B)|, where small values of Q are desirable, since div$B$ should ideally be zero. For highly non-regular tetrahedral shapes, however, the use of this indicator is less certain and typically Q is used only to indicate when the curlometer estimate is likely to be bad. In addition, the overall uncertainty in the linear approximation of both div$B$ and **curl**B also results from measurement errors in the magnetic field, spatial position and inter-spacecraft timing.

The redundant face of the tetrahedron can also indicate uncertainty in the calculation. The choice of three faces used in the calculation can be cycled using different reference spacecraft in Eq. 5.1 so that four different results can be obtained, verifying the sensitivity of the estimate for each Cartesian component of J (this then provides a way to assess uncertainty independently to the estimate of div$B$, and hence Q). Directly estimating the linear spatial gradients for each current density component; for example, from the dyadic of B, is identical to this original form of the curlometer (see Chap. 4), but the error handling (and hence relevant quality parameters) is slightly different and in the implementation of the equations above, the estimate is often self-stabilizing for common current structures such as sheets and tubes (Dunlop et al. 2002; Robert et al. 1998), because of the closed form of the integral equations.

Clearly, it will be the case that certain forms of structure may align with one or more components of the current density, often resulting in more accurate determination of that component. In fact, non-regular tetrahedral spacecraft configurations preferentially access some directions in space more accurately than others, and hence sample the components of the current preferentially (depending on alignment, or misalignment, to the dominant current direction and its form). When sampling large-scale currents at the magnetopause or magnetotail, for example, the effect of irregular configurations can be a significant drawback; but it can also be a benefit to the measurement of currents which are highly directed to the form of the background magnetospheric regions. Examples of these are the ring current, where the dominant current is azimuthal (Zhang et al. 2011) and field aligned currents (FACs), where one face of the tetrahedron formed by the spacecraft can be used to estimate the component of the current which is closest to the FAC direction (Dunlop et al. 2015b). In

general, however, the effect of spatial structure cannot be separated from that arising from temporal behaviour on time scales smaller than the natural convection time across the spacecraft array (see Sect. 5.2.2 for more discussion).

5.2.2 Cluster Lessons: Implementation, Scale Size and Stationarity

The implementation of the method from Eq. 5.1 is done with reference to the right hand side of Fig. 5.1, where it can be seen that the size of the current components perpendicular to each face of the tetrahedron can be found from the terms on the right hand side of Eq. 5.1 and the normals to each face (and hence the orientation of these current components) are obtained from $(\Delta \boldsymbol{R}_i \hat{} \Delta \boldsymbol{R}_j)/|(\Delta \boldsymbol{R}_i \hat{} \Delta \boldsymbol{R}_j)|$ on the left hand side of Eq. 5.1. Cartesian components can then be found from projections of three of these components onto X, Y, Z coordinates in the usual way. In order to make this computation from four-spacecraft data, the time series need to be interpolated onto a common timeline.

For the method to perform well, in general, the spatial configuration needs to be small compared to the characteristic scale size of the current structure to minimize the effect of the non-linear gradients (i.e. non-measured gradients in the current density) and therefore accurately compute actual current density. This condition, however, is limited by timing errors between spacecraft and the effect of the measurement errors in $\boldsymbol{B}$ and $\boldsymbol{R}$, which become more significant at smaller spatial scales. Thus, smaller tetrahedral scales require higher absolute accuracy in $\boldsymbol{B}$ and $\boldsymbol{R}$, and rapid temporal behaviour requires higher cadence and accuracy of the measurement times. For example, for the Cluster mission, the spacecraft separations were typically larger than a few 100 km and linearization errors dominated errors in the estimates, since measurement uncertainty (~0.1 nT in $\boldsymbol{B}$; a few km for $\boldsymbol{R}$ and millisecond timing) was low by comparison (for currents greater than a few nAm^{-2}). In the Cluster regime, therefore, Q is a reasonable quality indicator. By comparison, the typical spacecraft separations accessed by the MMS mission (Burch et al. 2016) are 10's of km so that the curlometer is likely to be more often in the linear regime where errors due to gradients in the current density are small. On these smaller spatial scales, however, the measurement errors could become significant unless the currents measured are large.

There is a further consideration on the calculation of the magnetic field differences in the context of the linear approximation. Although the method can be applied to the measured $\boldsymbol{B}$ point by point in time, the background field may itself contain strong non-linear gradients even though the background current density is zero (this is the case for the internal geomagnetic field, arising from the IGRF, dominated by the Earth's dipole field). In that case, the neglect of non-linear gradients in the linear estimates can imply non-physical (i.e. not real) currents (the effect is significant in the inner magnetosphere and therefore affects the ring current calculation, and

the calculation of FACs at low orbit for example). Thus, implied currents from the estimate will arise when the curlometer is applied to a geomagnetic model field in which the current is zero (such as the IGRF). This effect, first noted in Dunlop et al. (2002) was analysed in the context of the ring current more recently by Grimald et al. (2012). The curlometer can be applied to residual measured fields which result after first subtracting a zero-current model field from the measured magnetic field, however, and this minimises such effects. Indeed it is necessary in the high field regions of the magnetosphere and ionosphere (Yang et al. 2016; Dunlop et al. 2015). The use of a defined model field containing no current density is usually sufficient and of course it is usually desirable that any de-trending of the data in this way should not remove any real currents which may be present. Nevertheless, this does provide a way to separately analyse different current systems (such as large and small-scale effects) where some part of the current system is known or can be accurately modelled.

5.2.3   Key Regions Covered by Related Methodology

The curlometer method has proved to be robust and has been successfully applied in many different regions of the Earth's magnetosphere, such as the magnetopause (e.g. Dunlop et al. 2002, 2005; Haaland et al. 2004; Panov et al. 2006); the magnetotail current sheet (e.g. Runov et al. 2006; Nakamura et al. 2008; Narita et al. 2013); the ring current and inner magnetosphere (e.g. Vallat et al. 2005; Shen et al. 2014; Yang et al. 2016); field-aligned currents (FAC, e.g. Forsyth et al. 2008; Shi et al. 2010), and other transient signatures (e.g. Roux et al. 2015; Xiao et al. 2004; Shen et al. 2008), as well as to structures in the solar wind (e.g. Eastwood et al. 2002).

Methods which more generally estimate the gradient of the magnetic field have also been extensively applied to multi-spacecraft magnetic field measurements (Chanteur 1998; Harvey 1998; Vogt et al. 2008; Shen and Dunlop 2008) and methods based on calculation of the magnetic rotation rates to estimate field line curvature, as well as the current density directly, have also been developed (Shen et al. 2007, Dunlop and Eastwood 2008) and can be readily applied to irregular configurations of 3–5 spacecraft (Shen et al. 2012a, b). In addition, equivalent methods have been developed based on the use of planar reciprocal vectors (Vogt et al. 2008, and Chap. 4) and the method of least squares (e.g. DeKeyser et al. 2007; Hamrin et al. 2008). Although these methods have been predominantly applied to the outer magnetospheric regions (dayside magnetopause, magnetotail and lobes), where the influence of the Earth's internal field is weak and temporal fluctuations are often dominant, recently there have been a number of studies using multi-spacecraft estimates of current density in the inner magnetospheric regions and ring current (Vallat et al. 2005; Zhang et al. 2011; Shen et al. 2014), and in regions supporting field aligned currents (Marchaudon et al. 2009; Shi et al. 2010, 2011).

These methods (including the basic 'curlometer' above) are applicable to situations where less than four-spacecraft are closely grouped (Dunlop et al. 2016, 2018). With less than four-spacecraft, only a partial estimate of a single component of $\boldsymbol{J}$

(the component normal to the plane of the spacecraft) can be made unless other data sets are used in conjunction with the magnetic field, such as the plasma moments, or where assumptions in the behaviour of the currents can be made (e.g. stationarity of the field, known FACs or force free structures) in certain regions such as at low Earth orbit (e.g. Vogt et al. 2009, 2013; Shen et al. 2012a, b; Ritter and Lühr 2013, Dunlop et al. 2015a, b). Nevertheless, until the launch of the three Swarm spacecraft in 2014, altitudes at low-Earth orbit (LEO) had not benefited from multi-point measurements. In fact, the method can be generalised under certain assumptions of stationarity (see the applications below discussed in Sect. 5.4 and Chaps. 4 and 6).

The above outline represents the key issues revealed from the standard application of the method in many regions of near-Earth space since the launch of Cluster (see for instance Dunlop and Eastwood, (2008), for a review, and Dunlop et al. (2016, 2018), for a summary of the practical experience gained). Ready to use implementations of the curlometer method can be obtained from the Cluster Science archive (http://www.cosmos.esa.int/web/csa/software), and see the technical note by Middleton and Masson (2016).

5.3 Use of Cluster and THEMIS for in Situ Ring Current Surveys

The terrestrial ring current (RC) extends significantly in both latitude (-30 to 30 deg) and radially from about 2–7 R_E as a result of its variability in strength and location.

5.3.1 Application of Cluster Crossings to Survey the Ring Current

The curlometer has been applied to the RC using the in situ measurements of Cluster (Dandouras et al. 2018; Dunlop et al. 2018), which generally sampled the RC as the spacecraft passed through perigee during all phases of the mission. During the early to middle phase (2001–2009), the polar Cluster orbit passed normally through the ring current (at radial distances of ~4–4.5 R_E), as was first reported by Vallat et al. (2005) and later extended to full azimuthal coverage in local time (see the left hand side of Fig. 5.2) by Zhang et al. (2011). These studies found that the stability of the current density for each pass was such that the orientation of the Cluster configuration typically allows the azimuthal (ring plane) component, J_ϕ, to be estimated accurately, since the configuration often aligns perpendicularly to the ring plane. Cluster in fact also often samples FACs adjacent to the RC, where the alignment of J_N (the current component normal to the plane of the configuration) to $J_\parallel$ is significant, so that the occurrence of R2 FACs, which connect through the RC, can be inferred, in principle.
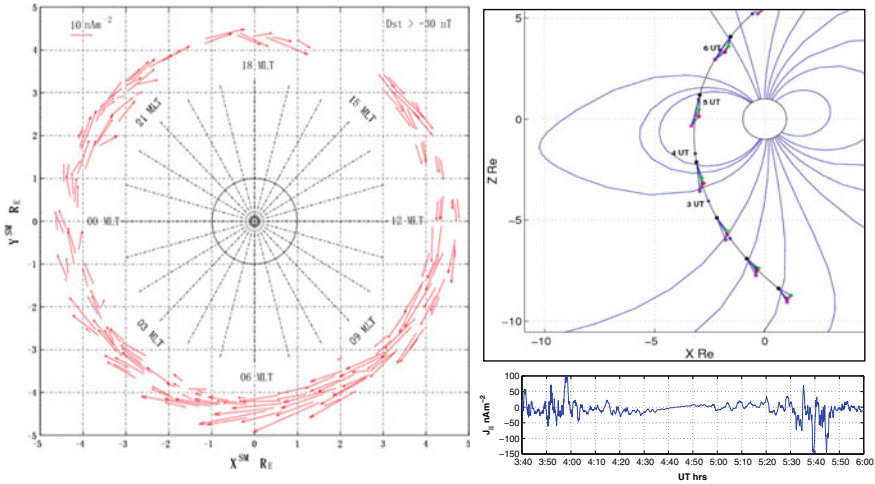
Fig. 5.2 (left) Full azimuth scan (magnetic local time, MLT) of ring current (RC) passes, plotted in solar magnetic (SM) coordinates (dipole aligned), and between -30° to 30° latitude (Zhang et al. 2011). The length and direction of the vectors represent ten minute averages of the current density obtained from the curlometer. The measurements represent non-storm (Dst > -30 nT) values of the RC. The RC strength is seen to increase with MLT on the dawn-side (03–12 MLT) and is a little suppressed on the dusk side. (right) The top plot shows a Cluster orbit relative to the magnetic field lines for a night-side perigee orientation where the configuration is oriented suitably to access the azimuthal ring current component and also is aligned normal to the field lines on exit from the RC. The lower plot shows the corresponding FA current density

The right hand side of Fig. 5.2 shows an orbit of Cluster, where the orientation of the Cluster configuration is suitable for sampling stable RC measurements as well as for the R2 FAC orientation as the spacecraft exit north and south of the ring plane. The lower panel of Fig. 5.2 shows that the field aligned component is zero within the core RC region (4:30–5:00 UT), but then starts showing FAC signatures at the RC edges and beyond. For large-scale current systems, such as the ring current, where the direction of the main current can be assumed, or for systems of known FACs, where the dominant current is along the known magnetic field direction, one face of the tetrahedron (i.e. three of the spacecraft) can often be selected to align closely to the main current. The crossing positions shown on the left hand side of Fig. 5.2 in fact statistically map to the equatorward boundary of the Auroral zone determined for Kp < 2 (non-storm activity) by Xiong et al. (2014), the R2 FAC intensity peaks.

5.3.2 Use of the Magnetic Rotation Analysis (MRA) Method for Field Curvature Analysis

In the in situ ring current, it is suitable to subtract the IGRF from the measured data in order to form magnetic field residuals for computation of the current density. This has been discussed by Shen et al. (2014), who also computed the magnetic field line curvature (using the MRA method) for a number of storm-time events. That study also showed a strengthening of the RC with storm activity, behaviour which was also reflected in the field-line curvature estimates. The magnetic field-line (MFL) curvature results are shown in Fig. 5.3 for the storm time events of Shen et al. (2014) as well as for the combined database of events with Zhang et al. (2011). The plots show that, based on estimates of the MFL curvature for events with sym-H activity levels down to around −50 nT, the dawn and night side (green and black) strengths are higher (smaller curvature) than the dayside and dusk events. At higher activity the situation is less clear, but the night side (black) population shows higher strengths (lower Rc) generally (this could be a result of sub-storm phase effects in this region). Nevertheless, this broadly is consistent with the curlometer statistics of Zhang et al. (2011).
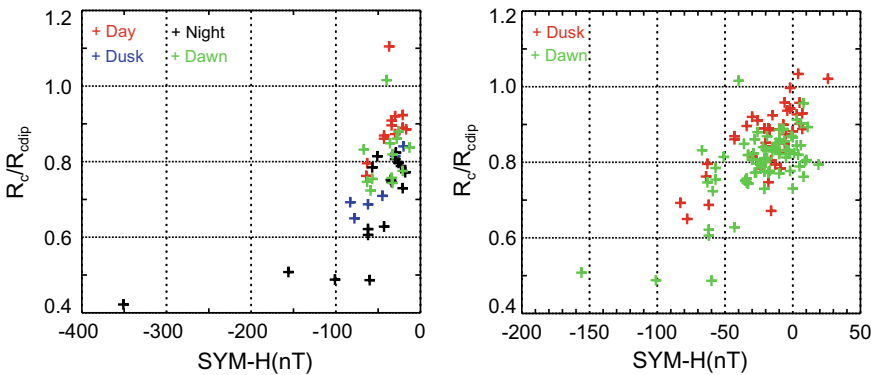

Fig. 5.3 Plots of MRA analysis of the magnetic field line curvature (Rc) estimates against sym-H activity. (left) The results for Cluster storm time RC crossings (after Shen et al. 2014), where the data are classified by local time sector (red, day; blue, dusk; green, dawn; black, night). (right) The combined statistics for both storm and non-storm conditions binned only with respect to two wide LT ranges: red (dawn + night) and green (dusk + day)

5.3.3 Use of THEMIS Three-Spacecraft Configurations to Sample the Ring Current

A further study has been carried out by Yang et al. (2016), using an application of the method of Shen et al. (2012) to the group of three magnetospheric THEMIS spacecraft, which often came into a close, 3-spacecraft configuration at times when they were providing coverage through the Earth's ring current. The geometry of the configurations is shown on the left hand side of Fig. 5.4 to illustrate that the current component normal to the configuration can be readily obtained, but generally takes some angle relative to the J_ϕ component (in the X,Y plane of the magnetic dipole equator). This geometry using only three-spacecraft is therefore useful in circumstances like this where the expected main current component is known.

The THEMIS azimuthal coverage is summarized on the right hand side of Fig. 5.4, where radial coverage is achieved from about 4 up to 12 R_E (i.e. a much larger range than for Cluster). The results were classified according to sub-storm phase and show both a clear radial profile for the recovery phase of each sub-storm period, and resolve the Eastward reverse current on the inner edge of the RC. The Eastward/westward ring current boundary is found to be at L = 5 on average, but is sensitive to storm activity. This coverage is unfortunately limited on the dawn-side so that LT trends are not well resolved in that sector. There is also a bias to strong storm events near midnight LT.
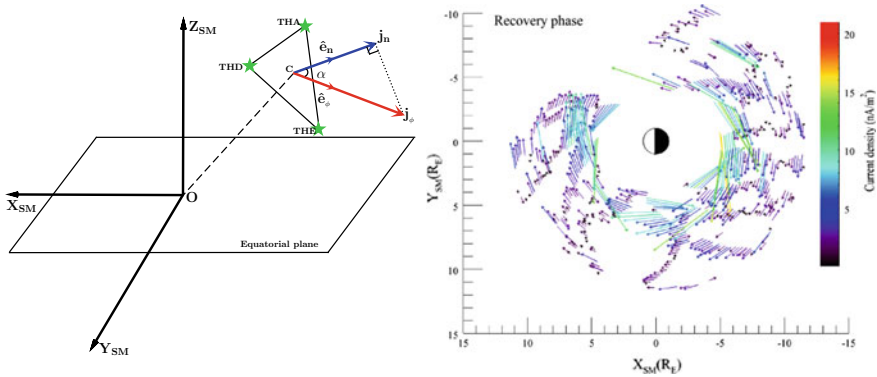
Fig. 5.4 (left) Application of the method of Shen et al. (2012) for the case of three THEMIS spacecraft (from Yang et al. 2016). (right) THEMIS coverage of the RC for current densities projected into the ring plane and for all storm activities during the recovery phase (i.e. outside the main phase of the storm)

### *5.3.4   Future Use of MMS and Swarm: Small Separations*

In fact, the MMS spacecraft, launched recently in 2015, also cover the ring current and comparisons may be made to these THEMIS measurements for the much smaller MMS separation scales, as well as the complementary Cluster coverage through the RC. All of these missions: MMS, THEMIS and Cluster are currently operating and can potentially extend these ring current surveys for the period covered by Swarm. The use of Swarm measurements can be carried out in two ways: either for event studies where conjunctions with both the RC and R2 FACs can be found with Swarm, or by statistically comparing in situ RC strength with corresponding RC terms in the model field derived from Swarm data (perhaps to show LT sensitivity).

5.4   Multi-spacecraft Analysis for Swarm: FACs

The multi-spacecraft techniques are applied as purely spatial estimates, point by point in time, but some magnetospheric phenomena are better suited to allow the temporal and spatial variations to be disentangled than others, depending on their properties and sampling resolution. In low altitude regions, however, studies have, until the launch of the three Swarm (Friis-Christensen et al. 2008) spacecraft (labelled A, B and C), relied on estimates arising from single spacecraft data, for which separation of temporal and spatial variations is particularly difficult (Lühr et al. 2015) unless some knowledge about the key properties of both large and small-scale field aligned currents (FACs) is assumed. As we describe below, these conditions can be relaxed in different ways depending on the spacecraft coverage achieved by the array of spacecraft. In principle, the Swarm mission provided the opportunity to perform direct estimates of current density through the multi-spacecraft techniques, removing at least some of the ambiguity arising from single-spacecraft methods, but then typically is limited to the larger scale currents with some degree of stationary properties.

The Swarm spacecraft were launched on 22 November 2013 into circular, polar, low-Earth orbits (LEO). After 17th April 2014, a final configuration was achieved in which the Swarm A and C spacecraft fly close together at ~100–150 km separation and at a mean altitude of about 481 km (giving an orbital period of ~94 min). Swarm B, is flying at a slightly higher orbit of ~531 km, with a slightly different orbital period of ~95 min (see Dunlop et al. 2015), where its orbital plane drifts relative to A and C. At the start of science operations, Swarm B was initially aligned with the orbital planes of A and C and the three-spacecraft flew close to each other at regular periods every few days. The polar orbits take the Swarm spacecraft through the auroral regions and across the polar cap at high latitudes and sample all local times in about 132 days (spacecraft A/C), similar to the coverage of the CHAMP spacecraft (Reigber et al. 2002).

In this high field region magnetic residuals are computed by first subtracting a high-resolution internal field model before application of the curlometer. If it is assumed that the magnetic field signals associated with the currents do not significantly evolve in time over the durations needed (~10–20 s) for the spacecraft to move to adjacent positions (such assumptions of stationarity of the field can typically be made at low Earth orbits and often actual time dependence can be mitigated by suitable low pass filtering of the data), then these adjacent positions can be combined with the current A, B, C positions to produce added measurement points, as depicted on the left-hand side of Fig. 5.5 (see full description in Sect. 5.4.1). Thus, the multi-point curlometer can in principle be applied from selections of any combination of positions (extending the work of Ritter et al. 2006, 2013), also described in Chap. 6). Different configurations of the combined positions can be characteristically either 2-D or 3-D and are associated with different effective mean times for the measurements so that the different choices of combinations of time-shifted spacecraft positions can test the temporal stability as well as the validity of the field-aligned component. Furthermore, in a similar manner to the choice of tetrahedral face in the standard application described in Sect. 5.3, the choices can indicate the stability and accuracy of the estimate (see also the discussion in Chap. 8). These considerations have been explored in two recent papers (Dunlop et al. 2015, 2015b), who estimated the current density at Swarm altitudes using 2–4 spacecraft positions, and showed that coordinated field aligned current (FAC) signatures can exist at both Cluster and Swarm and we provide an account of the methodology below in Sects. 5.4.1–5.4.3.
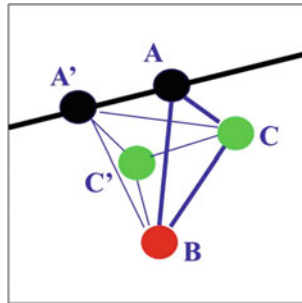
Fig. 5.5 Orbit track of the three Swarm spacecraft (A, B, C) when these are grouped closely together. The positions A', C' are of these spacecraft a few seconds earlier. When these are combined, giving up to five positions, then the full curlometer can be applied and all components of the current density, J, may be recovered (i.e. by using selected configurations of four spatial positions, e.g. A, A', B, C and using some mean time reference suitable for each configuration) (from Dunlop et al. 2015a, b)

5.4.1 Method: Application of the Curlometer to Stationary Signals

Chapter 6 outlines in detail the standard method of calculation of FACs, which uses the dual-spacecraft Swarm dataset and is applied to produce the standard Level 2 dual-spacecraft FAC data products using a specific implementation, and criteria on the field model used to construct residual magnetic field vectors. The dual-spacecraft method (Ritter et al. 2013), applies the curlometer in a modified form using only the two-spacecraft flying side by side, Swarm A and C, and therefore applies to most of the mission operations. The adaptation uses time shifted positions of A and C and seeks to optimise the alignment of the vertical current component linearly estimated from these positions to the FAC direction (i.e. to the expected background field direction).

Even when flying in close formation, the three Swarm spacecraft generally allow only a partial estimate of the current density (i.e. one component, normal to the plane of the configuration), unless these time shifted positions are used in combination with the current ABC positions. Figure 5.5 shows that the ABC positions, for some current time-step, are planar, but adding measurements at the positions (A' and C') for adjacent times (either earlier or later and typically shifted by 5–20 s to regularise the configuration) produces 3-D configurations. This provides a measurement set of up to 5 spatial points, from which the magnetic gradients (and curl B in particular) may be estimated. Other configurations result if the position of B is also time-shifted. It is a fundament assumption that temporal variations are slower than the sampling rate of the sampled magnetic structures at LEO, so that the magnetic field signals can be considered to be stationary for these short time periods and therefore that the adjacent positions of the spacecraft in time can be considered to sample the same current structure, thereby providing additional spatial positions.

Thus, if the spatial structure of the magnetic field is assumed to be stationary on short time scales of a few up to 20 s then adjacent (time-shifted) positions of the spacecraft can add to the number of spatial positions used to estimate the differences in the magnetic field between each position. These assumptions can be tested through the stability of the estimates for different configuration choices, but as mentioned the effect of temporal variations can be limited if the data is filtered to lower cadence. The curlometer method anyway resolves current only on the scale of the configuration and therefore the matched time scales are the convective scales across the spacecraft configuration. Furthermore, as mentioned earlier, at these low Earth altitudes, the internal geomagnetic field, which contains non-linear gradients, dominates, so that linear estimators of the currents should be applied to the residual fields, obtained following subtraction of the static (and current free) internal field (in the examples below we subtract the Chaos model field Olsen et al. 2014) in order to remove errors introduced by the neglect of the non-linear terms.

The method is applied to the possible configurations in Fig. 5.1, obtained by selecting different sets of positions, to produce 2, 3 and 4-spacecraft estimates of current density from the basic 3 spacecraft spatial configuration of Swarm. By selecting

planar groups of 3 or 4-spacecraft (as well as using the spatial array ABC), a 'curlometer' estimate can be made such that three-spacecraft positions essentially form one face of the tetrahedron shown in the right hand panel of Fig. 5.1 (the use of four-spacecraft positions recovers the full curlometer estimate). There are, in fact, 4 sets of four-spacecraft, involving spacecraft B, that can be formed from the 5 positions shown (the array AA'CC' is nearly planar so is not a usable fifth grouping; see below). In the case of four-spacecraft the quality parameter from the linear estimate of div(**B**)/curl(**B**) can also be estimated (Dunlop et al. 1988) as described in Sect. 5.3.

Thus, if three Swarm spacecraft are close together, as shown here, different tetrahedral configurations may be selected so that the five positions provide some redundancy in the calculation; allowing the quality of the estimate to be tested. In this case however, account must be taken of the fact that each 4-point configuration has a slightly different barycentre (and therefore a different mean time associated with the estimate). A number of additional points should be noted:

1. Time shifting AC results in a nearly planar configuration of four positions (AA'CC'), where only one component of the current density is found so that the field-aligned current in particular is only obtained from a projection onto the field-aligned direction of the component normal to the spacecraft plane containing the spacecraft positions. This is true for the standard 'dual satellite' Level 2 (L2) data product FAC_TMS_2F in the Swarm dataset, calculated from two-spacecraft (A and C) (Ritter et al. 2013).

2. The current density estimate resulting from each group of spacecraft, relates to a particular barycentre (centre of volume of the configuration, see Harvey et al. 1998), so that the combination of different groups of spacecraft refer to slightly different mean times. This allows the degree of stationarity of the measurement to be probed, in principle, through different choices of spacecraft (which have different mean times for the corresponding barycentre). For example, three-spacecraft combinations (such as ACC', AA'C etc.) can be selected and refer to slightly different mean times.

3. For the special case of the configuration in Fig. 5.5, both four and three-spacecraft estimates can be cross-compared. The array of Swarm A, B and C produces a purely spatial estimate, but is typically in a slightly tilted plane to the A, C orbit tracks and additionally corresponds to the leading time of measurement.

4. We have chosen to show results below from the configurations formed through time shifting the positions of A and C (as indicated in Fig. 5.5), since this produces the best alignment of the configurations to the L2, 2-spacecraft parameter, and of course it is expected that in this high latitude region the dominant currents will be field–aligned and therefore approximately perpendicular to the basic plane formed by AA'CC'. The alignment is less critical for the four-spacecraft estimates, but it is still useful to use this choice for the L2 comparisons (see later discussion).

5. A more generalised method of constructing (or measuring) the configuration can be devised, as studied in terms of homogeneity scales in the least squares approach discussed by De Keyser et al. (2007) (and see references therein), and

this could be used in future applications and compared to other gradient methods (see conclusions). Here, we benefit from the special context of the Swarm orbit geometry and natural alignment expected of the main FACs.

It is therefore instructive to compare the estimates found from different combinations and below the comparison of the various estimates for a number of events are shown.

5.4.2 Use of Special Configurations: 2-, 3-, 4-, 5-Point Analysis

To test the application of the curlometer to the Swarm data, events can be selected from the first phase of science operations (April–August 2014), when the alignment of the orbits allowed the three-spacecraft to repeatedly come close together. The data used is 1 Hz Swarm level 1b data (https://earth.esa.int/web/guest/swarm/data-access), taken by the vector field magnetometers (VFM, Friis-Christensen et al. 2008), but where these data have had the Earth's static, internal field removed using the CHAOS-4plus model (e.g. Olsen et al. 2014), although this was updated with the CHAOS-6 model for the re-testing summarised in Chap. 8, very little difference in the estimates resulted from the updating of the CHAOS model. The curlometer method is then applied to the residual field data.

As shown on the spacecraft orbits in Figs. 5.6 and 5.7, the optimum time-shift to best match all methods and optimally regularise the spatial configuration of the spacecraft is found to be 20 s. A convention is adopted where the time-shifted positions, A', C' are labelled A' = An (for forward shift in time) or Ap (for backward shift in time), and similarly for C'. The field-aligned components of the multi-spacecraft, curlometer estimates are compared in the top set of panels in Figs. 5.6 and 5.7 to the 2-spacecraft, time-shifted method of Ritter et al. (2013) (shown as L2, from the Swarm Level 2 product FAC_TMS_2F, derived using VFM measurements). This highlights both compatibility with L2 and the differences observed between estimates. The set shows different spacecraft groups, selected from the enlarged constellations on the right hand side of Figs. 5.6 and 5.7. This $J_\parallel$ component is taken from the projection of J_N in each three point case (so depends on the actual orientation of the plane of the configuration) and is the field aligned component of the vector current in the case of the 3-D 4-point arrays. The first FAC signature in Fig. 5.6 has been analysed recently by Dunlop et al. (2015).

The top panel of the upper plots in Fig. 5.6 shows that AApCC$_P$ (which is effectively a 2-D configuration) matches well to the signature obtained from the standard L2 2-spacecraft product. The line for L2 is broken for the interval 04:11–04:12:30 UT, indicating where the orbits crossover (first spacecraft B and then AC, as indicated in the left-hand orbit plots). The quality of the estimates is expected to be downgraded as the form of the spacecraft array changes dramatically. This in fact is reflected in the deviations between the estimates (a measure of quality) as this
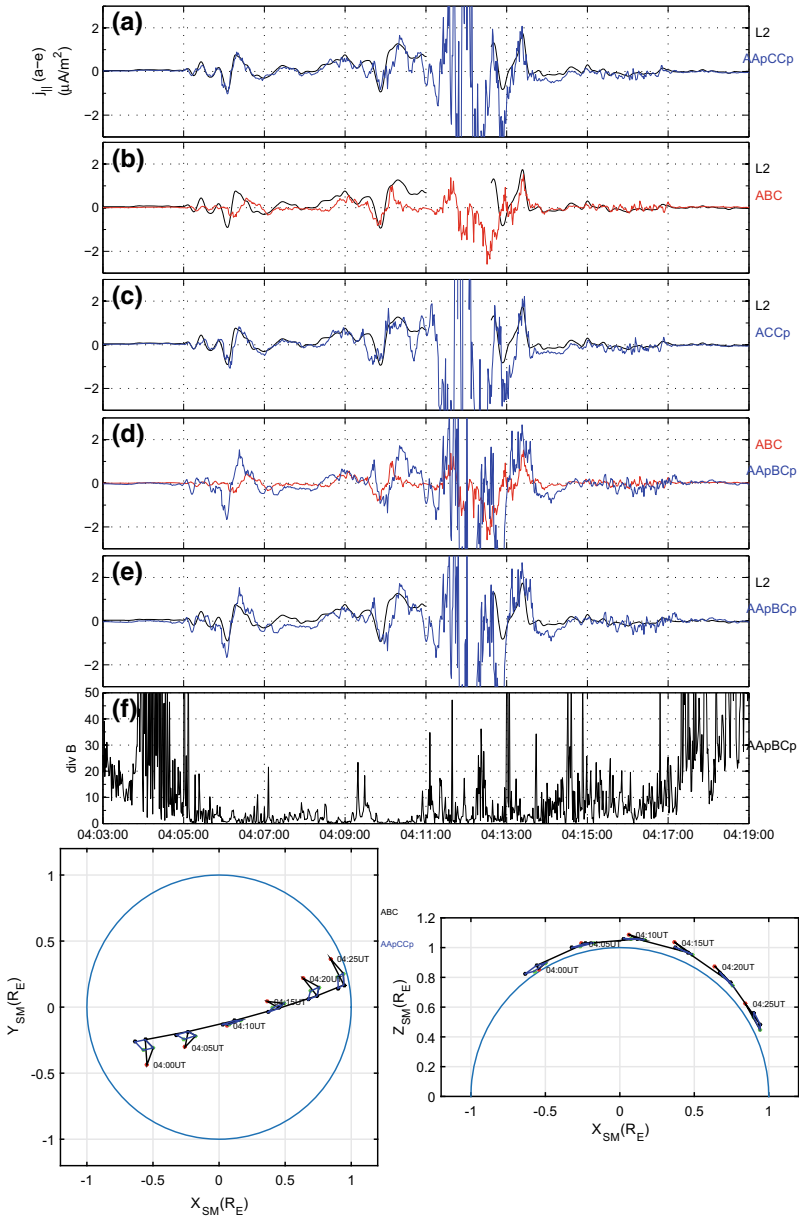
Fig. 5.6 The upper plot shows the set of curlometer estimates from selected configurations, for the 22 April 2014. From top to bottom, the panels show (the smoothed level 2 (L2) data product is shown as the black line): the 2-D 4-point array AApCCp; the three-spacecraft ABC spatial array (i.e. no time-shift, which has a different J_N direction); the three point array, ACCp; comparison of the 3-D 4-point array (AApBCp) with the ABC array and L2, respectively. The lowest panel shows the ratio div(B)/curl(B) (labelled divB for short) for AApBCp. The lower plots are orbit views (right, XY_{SM}, left, XZ_{SM}) with enlarged (x5) configurations as the Swarm spacecraft flew over the auroral zone and polar cap, where AC are time-shifted (from Dunlop et al. 2015)
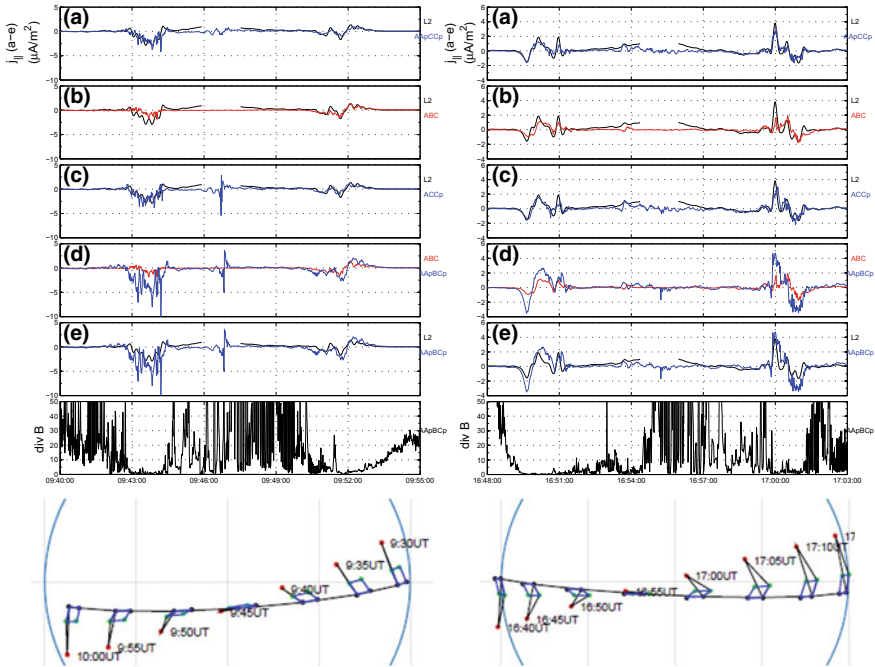
Fig. 5.7 The set of curlometer comparisons in the same format as Fig. 5.6, with the XY$_{SM}$ projections of the spacecraft configurations shown in the lower plots. The left hand plots correspond to the pass on 28 April 2014 and the right-hand to that of 4 May 2014

interval is approached and by the fluctuations in the estimates within the interval. Nevertheless, at other times, the profiles match in amplitude and approximate timing throughout the interval shown. This is as expected since the spacecraft positions (and hence plane of each configuration) is closely similar (the L2 parameter is smoothed and has a slightly different, shifted configuration to AA'CC'). The effect of different time-shift choices has most effect between 04:10-04:11 UT and 04:12:30-04:14 UT.

In the second panel, the relative tilt of the ABC plane (as seen in the XZ$_{SM}$ projection in Fig. 5.6) initially results in a lower amplitude FAC signal, since the projection of J_N is more misaligned to $J_\parallel$, for this configuration. Note, however, that the ABC estimate is a purely spatial estimate (linear gradients) which slightly changes the sampling of the FAC. These effects again evolve through the interval as the ABC configuration changes such that both the planar orientation (and hence the projection $J_\parallel$) and relative time of the corresponding barycentres changes along the orbit. The third panel shows that the use of only three positions, ACCp, also compares well with the L2 FAC signatures although some additional features are apparent. This estimate is sensitive to the choice of spacecraft positions since the effective barycentre time changes with each choice. Moreover, for ACCp as shown, the relative timing of the barycentre to that of the L2 estimate, changes along the orbit. In principle, this allows the quality of the L2 FAC estimate to be verified, i.e.

different choices for the three positions results in slightly different barycentre times relative to those of the L2 product, so that small temporal and spatial effects can in principle be revealed (these show up as small timing shifts in the traces because different configurations sample the FAC signature at slightly different times). There are 8 possible 3-spacecraft configurations which can be chosen relative to AApCCp or AAnCCn and these are summarised in Chap. 8.

The two lower panels in Fig. 5.2 show that the full curlometer estimate, arising from a 3-D 4-point array (here chosen as AApBCp) identifies the field-aligned signatures seen in the profile of the L2 product. In addition, the relative shifts in the profiles seen in the ABC estimate are confirmed to arise from that choice of configuration. The actual profile obtained for this 4-point estimate is sensitive to the choice of spacecraft positions and the resulting configuration, particularly for the field-aligned component which may align better with one or more of the faces of the configuration. The set of choices can therefore provide a further quality measure on the features observed, through the change in effective barycentre and different tetrahedral shape formed by each 4-position set. In principle, this can also be used to explore any effects of non-stationarity. For this event however, the profiles are broadly consistent. The $J_\parallel$ component for this configuration is actually obtained from the three vector components of current density (see Sect. 5.2) and so can be used even when the FAC direction deviates far from the plane of the spacecraft configurations. In fact, in both the lower panels, this estimate produces the highest amplitude FAC signal, suggesting that the L2 estimate (and that from the other three-spacecraft arrays) omits some of the actual FAC through the misalignment of J_N to the field aligned direction (see Sect. 5.4). The four-spacecraft estimate, despite incorporating two time-shifted positions, is in fact rather stable throughout the intervals tested and to those adjacent to the orbit crossovers in particular. It therefore provides additional coverage of signatures when the L2 product has low quality.

The bottom panel shows the standard estimate of div(**B**)/curl(**B**), which is obtainable for each choice of 4 positions (5 sets for each time-shift direction: forward and back). This parameter is only one measure of the quality of the linear gradients (see De Keyser et al. 2008), but it can be seen that this remains low throughout the intervals containing FAC signatures (where there is significant current). As such, this parameter does not absolutely indicate accuracy, but, as a rule of thumb, a value of 30% has previously been used as a threshold indicator of reliable current estimates. The value is large and shows high fluctuations in the regions at either end of the interval where the current is zero and also shows a significant increase during the period of orbit crossover (04:11–04:12:30 UT). This is therefore taken as a good indication of the overall quality of the estimates, although it only represents a measure of the non-linear gradients, not the absolute error or the effect of time dependence. The further choice of 4-spacecraft from the five (time-shifted) positions allows us to probe the effects of both the different spatial coverage (shape of the 4-spacecraft tetrahedron) achieved and time dependence through the different barycentre positions.

Two other events are shown in Fig. 5.7 for intervals extending across the polar passes in each case. On the left-hand side, corresponding to a pass on the 28 April 2014, the profiles are remarkably matched yet the increased amplitude of FACs caught

by the four-spacecraft estimate is pronounced, particularly for the signature between 09:42–09:45 UT. Note that div(**B**) is again very small during the key intervals of FACs, but shows low quality through the times adjacent to the orbit crossover, while the current density is very small. Similarly in the right panels, corresponding to the pass of the 4 May 2014, nearly all of the fine structure of the FACs is reproduced in all estimates providing confidence that these features are well represented. Again the amplitudes are caught best by the four-spacecraft estimates and in this case the ABC configuration is also well matched to the other profiles. The values of div(**B**) are similar to the previous event with low values during the FACs. In each event it is clear that despite the ABC estimate resulting from a pure spatial gradient, it suffers from the misalignment of the configuration plane to the true FAC direction so that the amplitude of this component is lower. The 3-D 4-point configurations appear to capture the true FAC amplitudes.

5.4.3   Use of the Extended 'Curlometer' with Swarm Close Configurations: 3-D Current Density

As described above, in the case of the basic, two-spacecraft method (and the other 2-D configurations) only the J_N current density component is obtained, so that any currents which are perpendicular to the magnetic field direction can only be seen through misalignment of the constellation plane to the background field. There may of course be errors introduced through lack of knowledge of the model field coordinates, but here the data defined coordinates are assumed. Figure 5.8 shows the vector current density estimates obtained from the 3-D 4-point estimates for key intervals during the 22 April and 4 May passes and for two different configuration choices. All components are in principle determined, so that $J_\parallel$ and $J_\perp$ can be directly computed. The main FAC signatures in each event are indicated and the characteristic forms for the other components can be seen in each case.

As indicated in Sect. 5.4.2, the FAC signatures broadly agree in form between each method, although the amplitudes of the 4-spacecraft curlometer are larger than the L2 parameter in some cases. A specific set of positions are shown in Fig. 5.8, based on time shifting the Swarm spacecraft A and C in order to remain as closely related to the L2 parameter as possible (as in Sect. 5.4.2). The character of the signatures does change slightly with each choice of four spatial positions (selected from the 5 positions depicted on the orbit plots of Figs. 5.6 and 5.7), but is most consistent for the optimum time shift giving the most regular configurations (in this case the value of div(**B**)/curl(**B**) is also predominantly insensitive to the choice of configuration). Indeed, the form of the signatures overall remains recognisable and in fact the change in each component seen for the different estimates between the top and bottom panels is less than 0.2 μAm^{-2} in the centre of the main current signatures (which range in magnitude from about 2–4 μAm^{-2}). This represents a maximum error in the estimates of around 10% due to changing the configuration.
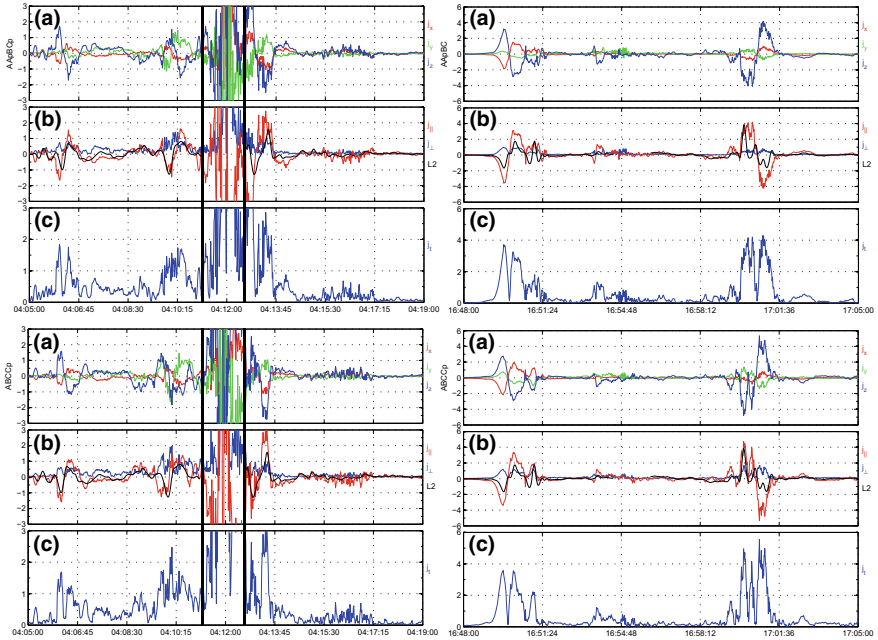
Fig. 5.8 Vector current density estimates obtained from the 4-point estimates for the key intervals during the 22 April (left) and 4 May (right) passes. For each event we plot the estimates from two configuration choices (top and bottom sets). For each plot, panel **a** (top) traces show the three SM components of the vector current; **b** (middle) traces show $J_{\parallel}$ and $J_{\perp}$, together with the L2 trace, and panel **c** (bottom) trace shows |J|. The estimates for the 22 April (left-hand panels) near the orbit crossover of Swarm A/C and B (between the vertical black lines) are unreliable due to distortion of the spacecraft configuration (from Dunlop et al. 2015)

For the interval on the 22 April we have also marked the region where the estimates will be unreliable due to the orbit crossover.

In each case, therefore, the perpendicular currents at either side of the FAC sheets are small but reach ~0.7 μAm^{-2} and thus are significant compared to the error. Furthermore, if the effect of changing the time-shift applied to the spacecraft positions is checked it is found that the perpendicular components remain significant although smaller time shifts, of 5 or 10 s, despite the severe distortion in the spatial configuration. For at least three of the signatures the perpendicular components show features which are consistent with the presence of perpendicular currents surrounding a FAC sheet (e.g. Gjerloev and Hoffman 2002; Liang and Liu 2007), i.e. reversals in the J_x and J_y components (SM coordinates) within the main FAC (see also Ritter et al. 2004; Wang et al. 2006). These signatures are not analysed but simply point out that the 4-spacecraft configuration can reveal perpendicular as well as parallel components. This was the first time these have been shown from direct measurements of the full vector current density at LEO, rather than as projections from single components (see Shore et al. 2013).

5.4.4   Current Sheet Orientation Implied by 2-Spacecraft Correlations

A complementary technique based on the cross-correlation of the single spacecraft estimates of FACs at each Swarm spacecraft has been recently introduced (Lühr et al. 2015; Yang et al. 2018), which results in estimates of the maximum correlation between sliding data intervals at two-spacecraft. The position of the maximum correlations found can be defined in terms of the required time shift (for example, from spacecraft A–C) and corresponding difference in the local time (this is given by the relative location of the spacecraft on the pair of orbits), and the correlation values can be computed as a function of local time (MLT) of the orbits. The results are found to depend on the level of filtering applied to the single spacecraft FAC data, and can identify different large-scale behaviour within broad regions characterised either by region 1 or region 2 currents.

An application of this information uses the positions of maximum correlations on the orbits to define the orientation of equivalent planer current sheets. These are estimated from the mid points of the maximum correlation intervals. If the sampled FACs are primarily large scale, then this can indicate the degree of order in the alignments (e.g. to the auroral oval). Conversely, if there are significant small-scale structures or fluctuations present then this will be reflected in unstable orientations and a lack of ordering. Figure 5.9 (adapted from Yang et al. 2018) shows the patterns in current sheet orientations found for intervals broadly associated with both region 1 and region 2 currents.
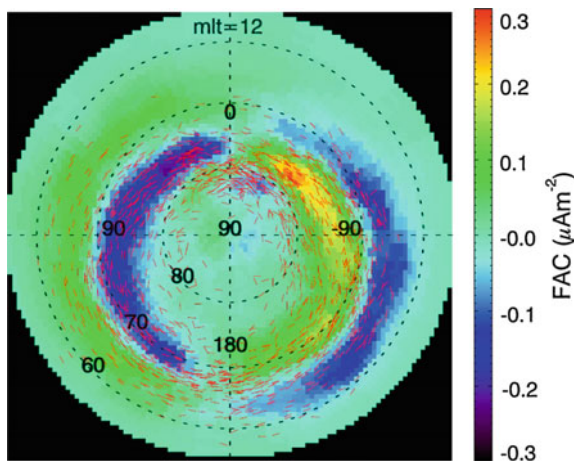
Fig. 5.9 Plot adapted from Yang et al. (2018), for a Northern hemisphere polar map, showing the average FACs for Swarm A and C data from 17th Apr. 2014 to 30th Apr. 2016, overlain with implied current sheet orientations for both higher latitude regions and lower latitude regions. These are plotted using lines of normalised length which connect the average Swarm A and C positions of those orbit segments producing the maximum correlations (drawn for 20 s filtered data)

## 5.5 Swarm-Cluster Coordination: FAC Scaling and Coherence

Although signatures of FACs, have been extensively reported (e.g. McPherron et al. 1973; Shiokawa et al. 1998; Cao et al. 2010), the form of the FACs, flowing along near-Earth field lines, has a highly time dependent signature, depending on their scale size, so that single spacecraft measurements cannot easily probe their nature. At more distant magnetospheric locations, multi-spacecraft analysis has been possible (e.g. Marchaudon et al. 2009; Slavin et al. 2008; Cheng et al. 2016), and indeed the distributed multi-spacecraft capability of AMPERE (Anderson et al. 2000), although limited in accuracy, is providing global features of FACs. The combined use of the multi-spacecraft Swarm and Cluster missions, however, allow the detailed resolution of individual FAC structure with close formations of spacecraft at both low and medium Earth orbits.

At the start of the Swarm operations in 2014, the four Cluster spacecraft were flying in tilted, eccentric orbits, with perigee heights ranging between 3 and 4 R_E. For several hours around perigee, Cluster passes through the Earth's ring current and often passes through the region of high latitude large-scale field aligned currents (FACs), particularly above the ring plane (magnetic equator). A study of possible coordination of Cluster operations with Swarm passes was carried out resulting in an adjustment of the Cluster configuration in order to optimise the Cluster tetrahedron as it passed through the Earth's ring current. This had the result that the configuration was also compact at perigee as large-scale FAC region was sampled. This special phase of Cluster operations therefore coincided with the first phase of Swarm operations when the three Swarm spacecraft repeatedly were grouped together as discussed in Sect. 5.3. The Swarm orbital planes drift relatively to Cluster at about 131 (spacecraft A/C) and 108 (spacecraft B) deg/year so that the alignment with the Cluster orbit slowly changes throughout the mission. This resulted in a number of multi-spacecraft conjunctions of Cluster with Swarm, during 2014, for which it was possible to match large-scale FAC signatures across different altitudes and identify the scaling properties.

One such conjunction is discussed below using the methodology described in Sect. 5.3. In addition, a recently developed method (Xiong et al. 2014; Xiong and Lühr 2014) is also used to identify crossings of the expected poleward and equatorward auroral boundaries (taken as the maximum gradient in R1 and R2 FAC power), where their statistical model of the form of these boundaries (derived from small and medium scale FAC using 10 years of CHAMP magnetic field data) is employed to help order both data sets. For the Cluster signatures, spin averaged data from the fluxgate magnetometers (FGM) (Balogh et al. 2001) is used.

5.5.1 Conjunction Characteristics

Figure 5.10 shows the combined locations of the spacecraft during the period of interest, which corresponds to the event described in Fig. 5.6. Cluster was flying from dawn to dusk through midnight local time during the few hours around 4:00 UT and passed from low to high invariant magnetic latitudes (MLAT) at around midnight local time, and at 2.5 R_E altitude, before falling again to low latitudes and passing through the magnetic equator (left panel). During part of this interval (~03:55–04:25 UT), the Swarm spacecraft flew through the auroral zone and across the polar cap in a close configuration (~100–150 km separation) of all three-spacecraft (see inset in the right hand panel). The Cluster configurations were such that three-spacecraft (1, 3 and 4) were close together (~1000 km separation) and in a plane nearly perpendicular to the magnetospheric field, while the fourth spacecraft, C2-red, lay further away (at ~5000 km separation from the others), allowing good resolution of the FACs at Cluster corresponding to the normal component to the 3-spacecraft plane. The Swarm configurations show the crossover of the orbits just after 04:10 UT (in a slightly different form to that shown in Fig. 5.6). The inset in the left hand panel also shows that Swarm and Cluster came into close magnetic alignment just before
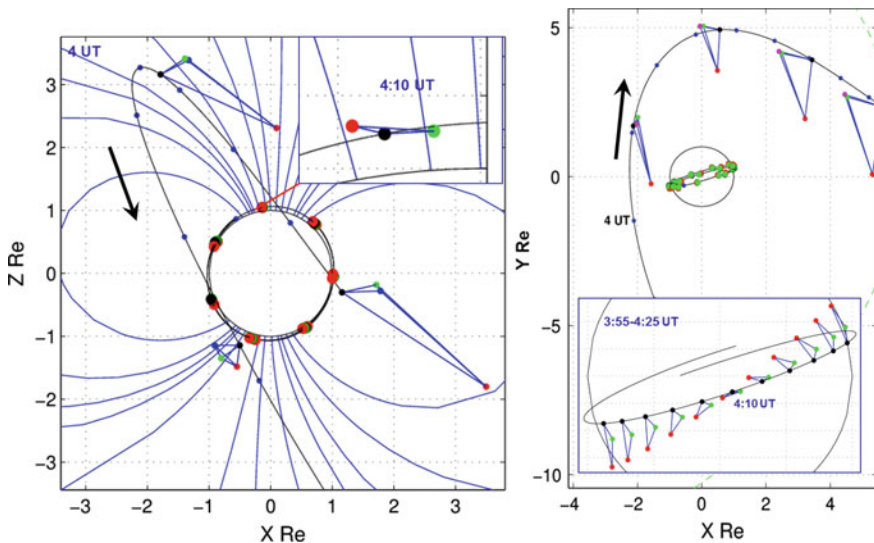
Fig. 5.10 Plot taken from Dunlop et al. (2015b), showing the orbits of Cluster and Swarm relative to the Earth in GSM coordinates on the 22 April 2014, projected into Z, X_{GSM} (left panel) and Y, X_{GSM} (right panel). The Earth is shown as a circle with model geomagnetic field lines shown for guidance in the Z, X projection. The Cluster configurations are shown enlarged by a factor of 3 relative to the orbit track of C1. The insets show zoomed views of the Swarm spacecraft configurations, projected into each plane, enlarged by a factor of 5 relative to the orbit of Swarm A. The Cluster colours are: C1-black, C2-red, C3-green and C4-blue, while the Swarm colours are: A-black, B-red and C-green

04:10 UT where Swarm flew under the magnetic footprint of Cluster, and shows the slightly higher altitude of the Swarm B spacecraft.

Figure 5.11 shows the ground mapped orbits of both Swarm and Cluster (we use ground magnetic footprints, from Tsyganenko, T89 model, (Tsyganenko 1989) to obtain a stable, relative position in both cases). These tracks confirm that the footprint of Swarm crosses the Cluster footprint between 4:05–04:07 UT. Also plotted are equatorward and poleward auroral boundaries, fitted statistically as ellipses to CHAMP data for different conditions by Xiong et al. (2014) and Xiong and Lühr (2014). These ellipses are plotted here for the times of the midpoints of the Swarm positions indicated by coloured dots on the Swarm orbit (Cluster positions are indicated by triangles). The method of Xiong et al. (2014), has been directly applied to the Swarm data for this interval, where the times indicated along the right hand Swarm track correspond to the actual estimates of the maximum gradient in FAC intensity. The mapped locations for Cluster 1, 3 and 4 cover the same scale as the Swarm array, so that the FACs are approximately covered on the same relative scale at each location.
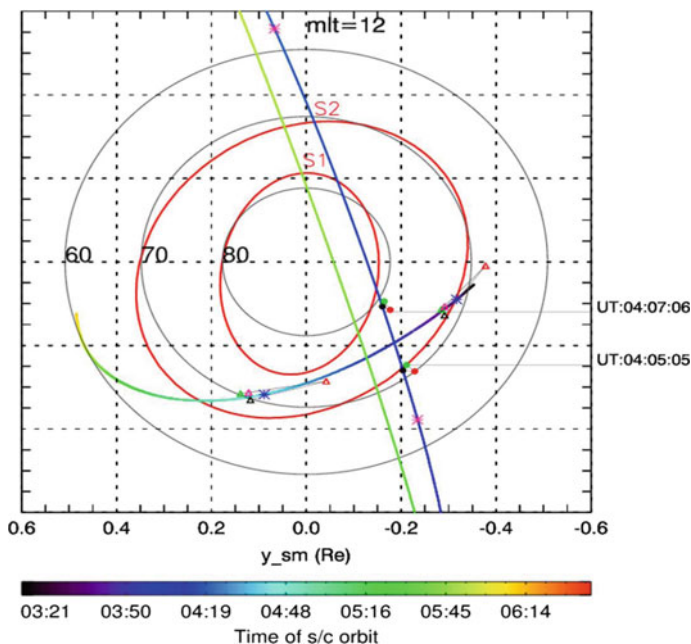
Fig. 5.11 Plot taken from Dunlop et al. (2015b), showing mapped footprints of Cluster and Swarm (where two passes are shown) in SM coordinates on the 22 April 2014, together with model, equatorward and poleward auroral boundaries, marked as S1 and S2 (referring to the expected locations of maximum R1 and R2 FA currents), which are taken from the fits in Eq. 5.8 of Xiong and Lühr (2014) after coordinate transformation. Also marked are times along the Swarm orbit for actual positions of the maximum gradients in FAC density (after Xiong et al. 2014)

The Cluster orbit is drawn from 03:40–05:00 UT, showing that Cluster moves from lower (~70°) to higher (~75°) MLAT, and back to lower MLAT, as it moves across MLT. Both the Cluster and Swarm tracks are colour coded with time to show that the orbits cross at about the same UT (Cluster crosses the MLT of Swarm a few minutes earlier than the Swarm flyover). The curlometer estimates for Cluster (not shown) confirm the spacecraft enter a region of negative parallel current, $J_{\parallel}$, as it approaches and crosses the S2 boundary just after 03:45 UT (at MLAT = 71°) and as it approaches the boundary again, crossing just after 04:55UT and at MLAT = 67° (consistent with the connectivity of R2 large-scale currents for this dawn-side local time). At the higher MLAT = 75° positions, Cluster approaches the S1 boundary where it shows zero or positive $J_{\parallel}$ (between ~04:00 and 04:15 UT).

Meanwhile for the first pass of Swarm (right track), the curlometer estimates for Swarm show the spacecraft also enter a region of FACs as the S2 boundary is crossed initially at 04:04 UT (MLAT = 71°). Signatures continue over the pass and are broadly consistent with the expected S1 and S2 boundaries as drawn, although other current systems are present (see Fig. 5.12, which shows the analysis of the period 03:40–04:20 UT, containing the first large-scale FAC at Cluster and the northern pass of Swarm). The terms large-scale and small-scale FACs below correspond to scale sizes at Swarm altitudes of >150 km and <150 km respectively.

5.5.2 Analysis of Common FAC Signatures

Figure 5.12 shows detailed estimates of the currents seen by Swarm using 1, 2, 3 and 4-spacecraft calculations taken from the configurations shown in Fig. 5.10. The third panel in each set shows the L2 product in black, the full 4 time-shifted spacecraft curlometer estimate in red, and the three-spacecraft estimate from the ABC configuration (in blue). The lower set of panels show the whole northern pass of Swarm (over the core time interval 04:03–04:19 UT), while the inset (upper panels) shows the first short burst of FACs on Swarm (during which Swarm crosses the Cluster orbit), between the ascending crossings of the S1/S2 boundaries (as indicated on the plot). Figure 5.11 shows that these boundary crossings correspond to the model boundary position for S2 and are near the position of the S1 boundary. The other vertical lines in the lower set of panels are drawn to mark different positions along the Swarm orbit: the dashed line at 04:11 UT corresponds to the position of the A/C and B orbit cross-over (as indicated in Fig. 5.10), while the A,C spacecraft cross at 04:12:30 UT, and the last vertical line at 04:14 UT corresponds to the first drop in size of the FACs (it also corresponds to the descending position of the S2 oval as drawn on Fig. 5.11).

These FAC estimates are best seen in the top set of panels, where the filtered single spacecraft signatures have similar, time-shifted profiles corresponding to the relative positions of spacecraft A, B and C as they cross the region: Swarm A and C are almost side-by-side, while Swarm B lags behind (~25 s). Swarm B, at a slightly higher altitude, sees a lower amplitude signature. In the lower panel, the 3-spacecraft
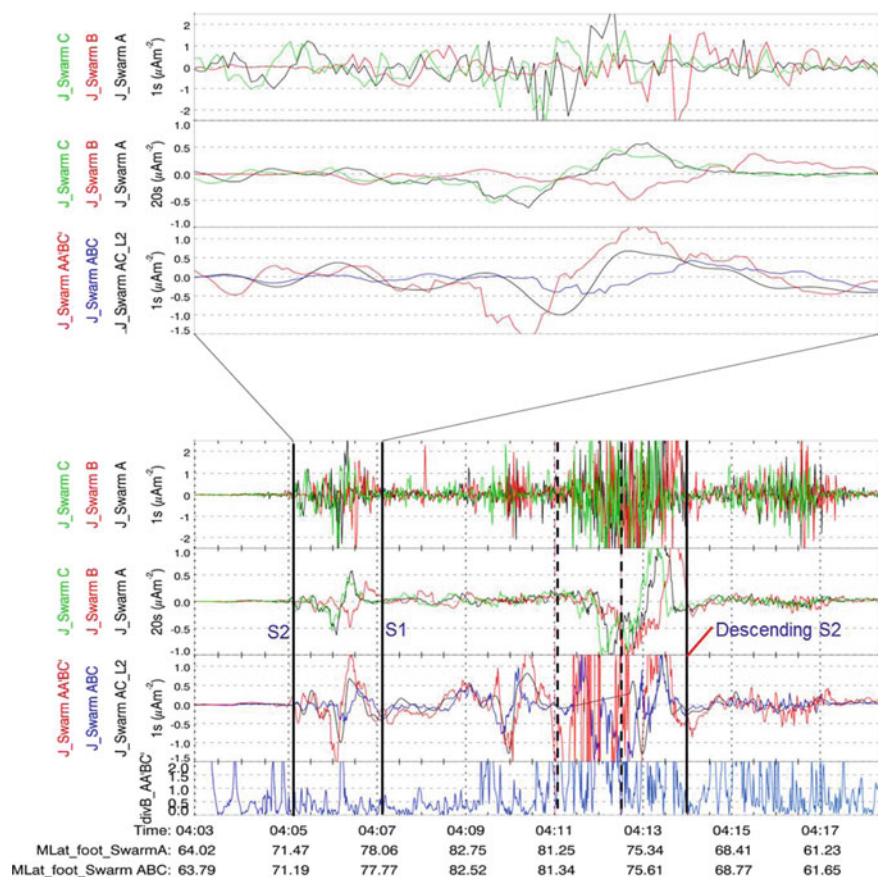
Fig. 5.12 Plot taken from Dunlop et al. (2015b), showing FAC estimates for Swarm for the whole northern pass (lower set) and for the intervals containing the ascending S2, S1 crossings (top set). In each set, the three panels represent (from the top): the level 2, single spacecraft estimates from dB/dt; the filtered single spacecraft estimates (20 s window), and the 2, 3 and 4-spacecraft curlometer estimates (as defined in Sect. 5.4). The ratios of div(B)/curl(B) obtained with the four-spacecraft estimate are also shown in the lowest panel, showing low values (high quality) for the key intervals containing the FACs

estimate (blue trace) gives the current normal to the ABC plane, which is tilted with respect to the FACs, so that its field aligned projection has low amplitude compared to that of the 4-point estimate (where the parallel component is taken from the full current density vector). The signatures of each estimate in the third panel are similar, but the profiles have relative time shifts since the barycentres of each are slightly different.

In Fig. 5.13 the Swarm and Cluster signatures are plotted in terms of their MLAT position to better compare these FAC features across altitude (~2–3 R_E). The Swarm plot corresponds to the time interval ~04:05–04:07:30 UT, containing the FACs seen
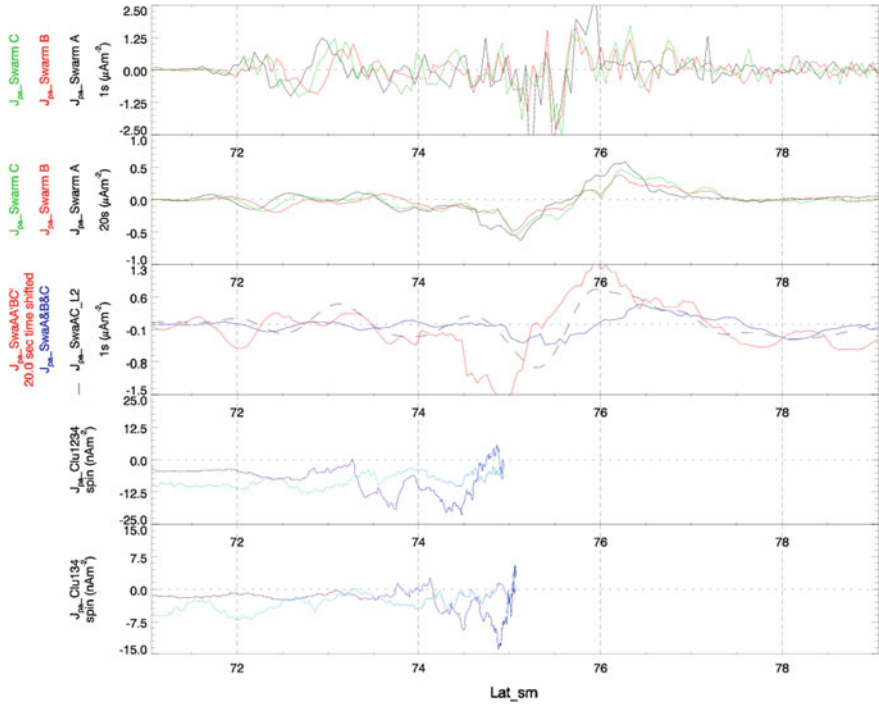
Fig. 5.13 Plot taken from Dunlop et al. (2015b), showing the mapped MLAT values (in SM coordinates) of Swarm and Cluster FACs. The top three panels correspond to the same set of FAC estimates as shown in the top set of panels in Fig. 4.3. The bottom two panels show Cluster FACs estimated by the full curlometer and from the face formed by C1, C3, C4 (which is almost perpendicular to the magnetic field), respectively. The light blue trace corresponds to the track of Cluster after the conjunction as it moves to lower latitudes, but far in local time from the Swarm track

between the S1 and S2 boundaries, while Cluster is plotted for the whole interval as it moves from MLAT = 71° and back again (03:30–04:40 UT). It needs to be borne in mind that there is a MLT difference between Cluster and Swarm which develops through the interval. Nevertheless, it can be seen that there are distinct features. For Swarm, the single spacecraft estimates contain two clear time independent signatures. The first is a large-scale (compared to the Swarm separations, i.e. approximately 150 km) feature between MLAT = 74° and 76° since it is sampled at the same position (MLAT) by each spacecraft as it flies through the FAC (the amplitude for the higher position of Swarm B is slightly reduced). The second (MLAT = 72° and 73°) is a small-scale structure since it is sampled at different MLAT positions by each spacecraft, implying limited (longitudinal) extent on the scale of the spacecraft separation.

It can further be seen in the third panel that the 3-spacecraft Swarm estimate derived from the ABC configuration (blue trace) broadly agrees with the Swarm

B signature in the second panel (i.e. that the estimate is driven by the swarm B location). Note that since the barycentres of the multi-spacecraft estimates differ slightly, there is no exact correspondence in MLAT. The Cluster signatures double back as the Cluster array moves from 71° to 75° (dark blue trace), and then back to 71° (light blue trace). The dark blue trace corresponds most closely in time with Swarm between 74° and 75° and shows a very similar profile in MLAT to the 4-spacecraft estimate from Swarm (red trace, third panel). The two Cluster estimates (from four and three-spacecraft calculation), serve to show the change in the effective location of the measurement when the inclusion of spacecraft 2 significantly shifts the effective mean position of Cluster.

Thus, the profiles show some similarity to Swarm and at similar MLAT positions, allowing for the slight shift in MLT between the spacecraft arrays. It is therefore probable that Cluster is sampling the same large-scale FAC as Swarm. The amplitudes of the FAC are also consistent: based on the expansion of the field lines, the field aligned current sheet cross-section should scale by about a factor of ~60 (ratio of field strengths) between the Swarm and Cluster altitudes. In fact, the amplitudes of current densities at Swarm and Cluster are ~1.3 μAm^{-2} and 20 nAm^{-2}, respectively, giving a ratio of ~65. The small-scale structure seen by Swarm at 73° would not be expected to map to Cluster positions in any coherent manner, and indeed there is no clear signature seen by Cluster at this position.

5.5.3   Other Events

A few other events during this phase of the Swarm mission have been analysed and show similar correspondences to those found above, even for intervals where there is a close conjunction with Cluster but no close grouping of the three Swarm spacecraft. In those cases particularly, but also generally, the Swarm signatures can be compared to the AMPERE model extracted for each event (see Chap. 7 for details of the AMPERE data taken from the Iridium spacecraft array) to clarify the characteristics of the large scale signatures. Unpublished analysis has suggested that filtered FAC signatures seen by Cluster can be mapped to the AMPERE altitudes, and can show similar large-scale features to the sampled AMPERE model currents, scaled to Cluster along the mapped orbit track.

5.6   Conclusions

Multi-spacecraft determination of currents, first from Cluster and later from the Swarm, Themis and MMS missions, has provided a wealth of new information about current structures in both the outer and inner magnetosphere. Despite the fact that for small-scale, time dependent current structures, the relative spacecraft separation and configuration, as well as magnetic field contributions from non-linear sources,

constrain the applicability of the method, the curlometer has proven to be a reliable and robust tool to determine both partial and 3D currents over a wide parameter range. Furthermore, estimates made from linear gradients tend to return average quantities which can be compared to other methods to probe neglected temporal or spatial effects. In addition, the application of temporal filtering (to reduce data cadence) and the removal of contributions to the magnetic field which contain non-linear spatial gradients (e.g. through subtraction of known model fields), can mitigate errors arising from these physical effects. As well as a review of the method, two key applications have been shown: to the Earth's ring current and to FACs, which benefit from such spatial and temporal filtering. These applications also show how the method can be tailored to sampling by fewer than four-spacecraft, where not all components of the current density can be computed without further assumptions.

The Earth's ring current has been extensively sampled by both Cluster and THEMIS and this chapter has shown a few sample studies in this regard. It is not intended as a complete review, but serves too show examples of the application. Cluster has allowed a full azimuthal scan of ring current crossings in a limited radial range, while allowing the ring current to be sampled above and below the ring plane, where the spacecraft can sample the adjacent FACs. Both the curlometer and the MFL curvature techniques have been applied and show evidence of dawn-dusk asymmetry in the ring current density. Cluster (and also THEMIS) has obtained coverage of the ring current in the period since the Swarm launch and it is likely that Cluster crossings in this era can be coordinated with Swarm to probe the MLT behaviour. Swarm can measure the ring current contributions to the geomagnetic field via the geomagnetic field modelling. The three magnetospheric THEMIS spacecraft measure the ring current for a wider range of radial distance, but do not sample well the regions above and below the ring plane. Both Cluster (because of often distorted spacecraft configurations) and THEMIS (since only three-spacecraft are flying together) rely on the ring current component of the current density being well determined. THEMIS also reveals effects of storm phase influence in the near-tail region which overlaps with the night-side ring current.

This chapter has also described a development of the curlometer technique to the low altitude region covered by Swarm, where the adoption of the principle of time-shifted measurements (in order to increase the number of spatial measurements of the magnetic field) can produce stable 2-, 3-, 4-point estimates of the electrical current density (a more general application of the method described in Chap. 6) which can be cross-compared. A set of estimates from the various possible configurations of positions which are sensitive to the barycentre time and position can be found. The range of estimates which follow have been applied along with other related methods to a standard event set to show the variability in the quantities found (see Chap. 8). The methodology used in this chapter can define a standard variance in the range of estimates as one measure of overall quality, but also comparison of the barycentre shifts and sampling can probe the degree of temporal and spatial variations of the event sampled, since the variance across the different configurations is dependent on this. Effectively, cross-comparison verifies the temporal effects as well as the inference of field aligned currents from the measured current components. Increased

stability of the signal measured from these alternative configuration choices gives confidence in the quality of the estimates and thus allows an increase in the coverage possible with valid estimates. Indeed the 3- and 4-spacecraft methods can show that the estimates can often be stable in intervals where the 2-spacecraft method breaks down. In the case of four-spacecraft configurations the full vector current can be resolved and provide a quality factor for the estimates directly. The spatial estimate of current requires the currents to be stable on time scales equivalent to the effective convection time of the spacecraft array across the structure. These time scales can be compared to the time shifts used and the time shift which produces the most regular configuration results in the optimal estimates of current density. Moreover, for the regions containing FACs, where the main current component is nearly perpendicular to the Swarm AC orbits (by operational design), it is natural to time shift the Swarm A and C positions. This produces configurations which relate most closely to the L2 FAC data product. Nevertheless, the estimate of div($\mathbf{B}$)/curl($\mathbf{B}$) was found to be relatively independent of the specific choice of 4-spacecraft configuration.

This chapter has also described how these methods have been applied to close magnetic conjunction between the Swarm and Cluster spacecraft arrays, where three Swarm spacecraft are flying in close formation and the Cluster configuration is elongated, but is well aligned to the background magnetic field direction. This data set therefore allows detailed, multi-spacecraft analysis of the magnetic field measurements at both the Swarm and Cluster locations. The combined data therefore identifies the spatial form of the large scale field-aligned current density at both low (~500 km altitude) Earth orbit and at higher altitudes of ~2.5 Re.

References

Anderson, B.J., K. Takahashi, and B.A. Toth. 2000. Sensing Global Birkeland currents with Iridium engineering magnetometer data. *Geophysical Research Letters* 27: 4045–4048.

Balogh, A., C.M. Carr, M.H. Acuña, M.W. Dunlop, T.J. Beek, P. Brown, K.-H. Fornacon, E. Georgescu, K.-H. Glassmeier, J. Harris, G. Musmann, T. Oddy, and K. Schwingenschuh. 2001. The cluster magnetic field investigation: Overview of in-flight performance and initial results. *Ann. Geo Cluster special issue* 19: 1207–1218.

Burch, J.L., T.E. Moore, R.B. Torbert, and B.L. Giles. 2016. Magnetospheric multiscale overview and science objectives. *Space Science Reviews* 5: 1–17. https://doi.org/10.1007/s11214-015-0164-9.

Chanteur, G. 1998. Spatial interpolation for four spacecraft: Theory, in analysis methods for multispacecraft data', *ISSI Science Report*, 395–418, SR-001, Kluwer Academic Pub.

Cheng, Z.W., J.C. Zhang, J.K. Shi, L.M. Kistler, M. Dunlop, I. Dandouras, and A. Fazakerley. 2016. The particle carriers of field-aligned currents in the Earth's magnetotail during a substorm. *Journal of Geophysical Research: Space Physics* 121: 3058–3068. https://doi.org/10.1002/2015JA022071.

Cao, J.-B., C. Yan, M. Dunlop, H. Reme, I. Dandouras, T. Zhang, D. Yang, A. Moiseyev, S.I. Solovyev, Z.Q. Wang, A. Leonoviche, N. Zolotukhina, and V. Mishin. 2010. Geomagnetic signatures of current wedge produced by fast flows in a plasma sheet. *Journal Geophysical Research* 115: A08205. https://doi.org/10.1029/2009JA014891.

Dandouras, I., S. Rochel-Grimald, C. Vallat, M. Dunlop. 2018. Terrestrial ring current: a review of cluster results based on the curlometer. In *Electric currents in geospace and beyond* (eds. A. Keiling, O. Marghitu, and M. Wheatland), John Wiley & Sons, Inc, Hoboken, N.J., *AGU books*. https://doi.org/10.1002/9781119324522.ch8.

De Keyser, J., F. Darrouzet, M.W. Dunlop, and P.M.E. Decreau. 2007. Least-squares gradient calculation from multi-point observations of scalar and vector fields: Methodology and applications with Cluster in the plasmasphere. *Ann Geo's* 25: 971–987. https://doi.org/10.5194/angeo-25-971-2007.

Dunlop, M.W., D.J. Southwood, K.-H. Glassmeier, and F.M. Neubauer. 1988. Analysis of multi-point magnetometer data. *Advances in Space Research* 8: 273–277. https://doi.org/10.1016/0273-1177(88)90141-X.

Dunlop, M.W., et al. 2002. Four-point Cluster application of magnetic field analysis tools: The Curlometer. *Journal Geophysical Research* 107 (A11): 1384. https://doi.org/10.1029/2001JA005088.

Dunlop, M.W., and A. Balogh. 2005. Magnetopause current as seen by Cluster. *Annales Geophysicae* 23 (3): 901–907. https://doi.org/10.5194/angeo-23-901-2005.

Dunlop, M.W., and J.P. Eastwood. 2008. The Curlometer and other gradient based methods. In *Multi-spacecraft analysis methods revisited'*, eds. G. Paschmann and P.W. Daly, *ISSI Science Report*, **SR-008,** pp. 17–21, Kluwer Academic Pub.

Dunlop, M.W., Y.-Y. Yang, J-Y. Yang, H. Lühr, C. Shen, N. Olsen, Q.-H. Zhang, Y.V. Bogdanova, J.-B. Cao, P. Ritter, K. Kauristie, A. Masson and R. Haagmans. 2015. Multi-spacecraft current estimates at Swarm. *Journal of Geophysical Research* 120. https://doi.org/10.1002/2015ja021707.

Dunlop, M.W., J.-Y. Yang, Y.-Y. Yang, C. Xiong, H. Lühr, Y.V. Bogdanova, C. Shen, N. Olsen, Q.-H. Zhang, J.-B. Cao, H.-S. Fu, W.-L. Liu, C.M. Carr, P. Ritter, A. Masson, and R. Haagmans. 2015b. Simultaneous field-aligned currents at Swarm and Cluster satellites. *Geophysical Reseach Letters* 42: 3683–3691. https://doi.org/10.1002/2015GL063738.

Dunlop, M.W., S. Haaland, C.P. Escoubet, and X.-C. Dong. 2016. Commentary on accessing 3-D currents in space: Experiences from Cluster. *Journal Geophysical Research* 121: 7881–7886. https://doi.org/10.1002/2016JA022668.

Dunlop, M.W., S. Haaland, X-C. Dong, H. Middleton, P. Escoubet, Y-Y. Yang, Q-H Zhang, J-K. Shi and C.T. Russell. 2008. Multi-point analysis of current structures and applications: Curlometer technique. In *Electric currents in geospace and beyond* (ed. A. Keiling, O. Marghitu, and M. Wheatland), John Wiley & Sons, Inc, Hoboken, N.J., *AGU books*, 2018, https://doi.org/10.1002/9781119324522.ch4.

Escoubet, C.P., M. Fehringer, and M. Goldstein. 2001. Introduction: the Cluster mission. *Annales Geophysicae* 19: 1197–1200. https://doi.org/10.5194/angeo-19-1197-2001.

Eastwood, J.P., A. Balogh, M.W. Dunlop, and C.W. Smith. 2002. Cluster observations of the heliospheric current sheet and an associated magnetic flux rope and comparisons with ACE. *Journal Geophysical Research* 107 (A11): 1365. https://doi.org/10.1029/2001JA009158.

Forsyth, C. et al. 2008. Observed tail current systems associated with bursty bulk flows and auroral streamers during a period of multiple substorms. *Annales Geophysicae* 26. https://doi.org/10.5194/angeo-26-167-2008.

Friis-Christensen, E., H. Lühr, D. Knudsen, and R. Haagmans. 2008. Swarm—An earth observation mission investigating geospace. *Advances in Space Research* 41: 210–216. https://doi.org/10.1016/j.asr.2006.10.008.

Gjerloev, J.W., and R.A. Hoffman. 2002. Currents in auroral substorms. *Journal of Geophysical Research* 107 (A8). https://doi.org/10.1029/2001ja000194.

Grimald, S., I. Dandouras, P. Robert, and E. Lucek. 2012. Study of the applicability of the curlometer technique with the four Cluster spacecraft in regions close to Earth. *Annales Geophysicae* 30: 597–611. https://doi.org/10.5194/angeo-30-597-2012.

Haaland, S., B.Ö. Sonnerup, M. Dunlop, E. Georgescu, G. Paschmann, B. Klecker, and A. Vaivads. 2004. Orientation and motion of a discontinuity from Cluster curlometer capability: Minimum variance of current density. *Geophysical Research Letters* 31: L10804–L10804. https://doi.org/10.1029/2004GL020001.

Hamrin, M. et al. 2008. Ann. Geo.

Harvey, C.C. 1998. Spatial gradients and the volumetric tensor. In *Analysis methods for multispacecraft data', ISSI Science Report*, 395–418, SR-001, Kluwer Academic Pub.

Henderson, P.D. et al. 2008. The relationship between j and Pe in the magnetotail plasma sheet: Cluster observations. *Journal of Geophysical Research* 113: A07S31. https://doi.org/10.1029/2007ja012697, https://doi.org/10.1029/2007ja012697.

Kivelson, M., and C.T. Russell 1995. *Introduction to space physics*. Cambridge University Press.

Liang, J., and W.W. Liu. 2007. A MHD mechanism for the generation of the meridional current system during substorm expansion phase. *Journal Geophysical Research* 112: A09208. https://doi.org/10.1029/2007JA012303.

Lühr, H., J. Park, J.W. Gjerloev, J. Rauberg, I. Michaelis, J.M.G. Merayo, and P. Brauer. 2015. Field-aligned currents' scale analysis performed with the Swarm constellation. *Geophysical Research Letters* 42. https://doi.org/10.1002/2014gl062453.

Marchaudon, A., J.-C. Cerisier, M.W. Dunlop, F. Pitout, J.-M. Bosqued, and A.N. Fazakerley. 2009. Shape, size, velocity and field-aligned currents of dayside plasma injections: a multi-altitude study. *Annales Geophysicae* 27: 1251–1266. https://doi.org/10.5194/angeo-27-1251-2009.

McPherron, R.L., C.T. Russell, and M.P. Aubry. 1973. Satellite studies of magnetospheric substorms on August 15, 1968: 9. Phenomenological model for substorms. *Journal of Geophysical Research* 78 (16): 3131–3149. https://doi.org/10.1029/ja078i016p03131.

Middleton, H.R. and A. Masson. 2016. The Curlometer Technique: a beginner's guide, ESA Technical Note ESDC-CSA_TN_0001, http://www.cosmos.esa.int/web/csa/multi-spacecraft.

Nakamura, R., W. Baumjohann, M. Fujimoto, Y. Asano, A. Runov, C. Owen, A. Fazakerley, B. Klecker, H. Rème, and E. Lucek. 2008. Cluster observations of an ion-scale current sheet in the magnetotail under the presence of a guide field. *Journal Geophysical Research* 1978–2012: 113. https://doi.org/10.1029/2007JA012760.

Narita, Y., R. Nakamura, and W. Baumjohann. 2013. Cluster as current sheet surveyor in the magnetotail. *Annales Geophysicae* 31: 1605–1610. https://doi.org/10.5194/angeo-31-1605-2013.

Olsen, N., H. Lühr, C.C. Finlay, T.J. Sabaka, I. Michaelis, J. Rauberg, and L. Tøffner-Clausen. 2014. The CHAOS-4 Geomagnetic Field Model. *Geophysical Journal International* 197: 815–827. https://doi.org/10.1093/gji/ggu033.

Panov, E., J. Büchner, M. Fränz, A. Korth, Y. Khotyaintsev, B. Nikutowski, S. Savin, K.-H. Fornaçon, I. Dandouras, and H. Reme. 2006. Cluster spacecraft observation of a thin current sheet at the Earth's magnetopause. *Advances in Space Research* 37 (7): 1363–1372. https://doi.org/10.1029/2006GL026556.

Petrukovich, A., et al. 2015. Current sheets in the earth magnetotail: Plasma and magnetic field structure with cluster project observations. *Space Science Reviews* 188: 311–337. https://doi.org/10.1007/s11214-014-0126-7.

Reigber, C., H. Lühr, and P. Schwintzer. 2002. CHAMP mission status. *Advances in Space Research* 30 (2): 129–134.

Ritter, P., H. Lühr, A. Viljanen, O. Amm, A. Pulkkinen, and I. Sillanpää. 2004. Ionospheric currents estimated simultaneously from CHAMP satellite and IMAGE ground-based magnetic field measurements: A statistical study at auroral latitudes. *Annales Geophysicae* 22: 417–430.

Ritter, P., and H. Lühr. 2006. Curl-B technique applied to Swarm constellation for determining field-aligned currents. *Earth Planets Space* 58: 463–476.

Ritter, P., H. Lühr, and J. Rauberg. 2013. Determining field-aligned currents with the Swarm constellation mission. *Earth Planets Space* 65: 1285–1294. https://doi.org/10.5047/eps.2013.09.006.

Robert, P., M.W. Dunlop, A. Roux, and G. Chanteur. 1998. Accuracy of current density determination. In *Analysis methods for multispacecraft data', ISSI Science Report*, 395–418, SR-001, Kluwer Academic Pub.

Roux, A., P. Robert, D. Fontaine, O. LeContel, P. Canu, and P. Louarn. 2015. What is the nature of magnetosheath FTEs? *JGR* 120 (6): 4576–4595. https://doi.org/10.1002/2015JA020983.

Runov, et al. 2006. Local structure of the magnetotail current sheet: 2001 Cluster observations. *Annales Geophysicae* 24: 247–262. https://doi.org/10.5194/angeo-24-247-2006.

Russell, C.T., J.G. Luhmann, and R.J. Strangeway. 2016. *Space physics: An introduction*. 978-1107098824, Cambridge University Press.

Shen, C., X. Li, M. Dunlop, Q.Q. Shi, Z.X. Liu, E. Lucek, and Z.Q. Chen. 2007. Magnetic field rotation analysis and the applications. *Journal Geophysical Research* 112: A06211. https://doi.org/10.1029/2005JA011584.

Shen, C., and M.W. Dunlop, in Multi-spacecraft analysis methods revisited', eds. G. Paschmann and P.W. Daly, ISSI Science Report, **SR-008**, 27–30, Kluwer Academic Pub.

Shen, C. et al. 2008. Flattened current sheet and its evolution in substorms. *Journal of Geophysical Research* 113, A07S21. https://doi.org/10.1029/2007ja012812.

Shen, C., J. Rong, M. Dunlop, Y.H. Ma, G. Zeng, and Z.X. Liu. 2012a. Spatial gradients from irregular, multiple-point spacecraft configurations. *Journal Geophysical Research* 117: A11207. https://doi.org/10.1029/2012JA018075.

Shen, C., Z.J. Rong, and M. Dunlop. 2012b. Determining the full magnetic field gradient from two spacecraft measurements under special constraints. *Journal Geophysical Research* 117: A10217. https://doi.org/10.1029/2012JA018063.

Shen, C., et al. 2014. Direct calculation of the ring current distribution and magnetic structure seen by Cluster during geomagnetic storms. *Journal Geophysical Research* 119: 2458–2465. https://doi.org/10.1002/2013JA019460.

Shi, J.K. et al. 2010. South-north asymmetry of field-aligned currents in the magnetotail observed by Cluster. *Journal of Geophysical Research* 115. https://doi.org/10.1029/2009ja014446.

Shi, J.-K., J. Guo, M. Dunlop, T. Zhang, Z.X. Liu, E. Lucek, A. Fazakereley, H. Reme, and I. Dandouras. 2011. Inter-hemispheric asymmetry of the dependence of cusp location on dipole tilt: Cluster observations. *Journal Geophysical Research* 30 (21–26): 2012. https://doi.org/10.5194/angeo-30-21-2012.

Shiokawa, K., et al. 1998. High-speed ion flow, substorm current wedge and multiple Pi2 pulsations. *Journal Geophysical Research* 103 (A3): 4491–4507. https://doi.org/10.1029/97JA01680.

Shore, R.M., K.A. Whaler, S. Macmillan, C. Beggan, N. Olsen, T. Spain, and A. Aruliah. 2013. Ionospheric midlatitude electric current density inferred from multiple magnetic satellites. *Journal Geophysical Research* 118: 5813–5829. https://doi.org/10.1002/jgra.50491.

Slavin, J.A., G. Le, R.J. Strangeway, Y. Wang, S.A. Boardsen, M.B. Moldwin, and H.E. Spence. 2008. Space technology 5 multipoint measurements of near-Earth magnetic fields: Initial results. *Geophysical Reseach Letters* 35: L02107. https://doi.org/10.1029/2007GL031728.

Tsyganenko, N.A. 1989. A magnetospheric magnetic field model with a warped tail current sheet. *Planetary and Space Science* 37: 5–20.

Vallat, C., et al. 2005. First current density measurements in the ring current region using simultaneous multi-spacecraft CLUSTER-FGM data. *Annales Geophysicae* 23: 1849–1865. https://doi.org/10.5194/angeo-23-1849-2005.

Vogt, J., G. Paschmann, and G. Chanteur. 2008. Reciprocal vectors. In *Multi-Spacecraft analysis methods revisited,* eds. G. Paschmann and P.W. Daly, ISSI Science Report, **SR-008**, 27–30, Kluwer Academic Pub.

Vogt, J., A. Albert, and O. Marghitu. 2009. Analysis of three-spacecraft data using planar reciprocal vectors: Methodological framework and spatial gradient estimation. *Annales Geophysicae* 27: 3249–3273. https://doi.org/10.5194/angeo-27-3249-2009.

Vogt, J., E. Sorbalo, M. He, and A. Blagau. 2013. Gradient estimation using configurations of two or three spacecraft. *Annales Geophysicae* 31: 1913–1927. http://www.ann-geophys.net/31/1913/2013/.

Wang, H., S.Y. Ma, H. Lühr, Z.X. Liu, Z.Y. Pu, C.P. Escoubet, H.U. Frey, H. Réme, and P. Ritter. 2006. Global manifestations of a substorm onset observed by a multi-satellite and ground station network. *Annales Geophysicae* 24: 3491–3496. https://doi.org/10.5194/angeo-24-3491-2006.

Xiao et al. 2004. Inferring of flux rope orientation with the minimum variance analysis technique. *Journal of Geophysical Research* 109. https://doi.org/10.1029/2004ja010594.

Xiong, C., H. Lühr, H. Wang, and M.G. Johnsen. 2014. Determining the boundaries of the auroral oval from CHAMP field-aligned currents signatures—Part 1. *Annales Geophysicae* 32 (609–622): 2014. https://doi.org/10.5194/angeo-32-609-2014.

Xiong, C., and H. Lühr. 2014. An empirical model of the auroral oval derived from CHAMP field-aligned current signatures—Part 2. *Annales Geophysicae* 32 (623–631): 2014. https://doi.org/10.5194/angeo-32-623-2014.

Yang, J.-Y., M. Dunlop, C. Xiong, H. Lühr, Y-Y. Yang, J.-B. Cao, J Wild, L-Y Li, Y-D Ma, H-S Fu, W-L. Liu, and P. Ritter. 2018. Statistical correlations of field-aligned currents measured by Swarm. submitted to *Journal of Geophysical Research*.

Yang, Y.-Y., C. Shen, M. Dunlop, Z.-J. Rong, X. Li, V. Angelopolous, Z.-Q. Chen, G.-Q. Yan and Y. Ji. 2016. Storm time current distribution in the inner magnetospheric equator: THEMIS observations. *Journal of Geophysical Research* 120. https://doi.org/10.1002/2015ja022145.

Zhang, Q.-H., M.W. Dunlop, M. Lockwood, R. Holme, Y. Kamide, W. Baumjohann, R.-Y. Liu, H.-G. Yang, E.E. Woodfield, H.-Q. Hu, B.-C. Zhang, and S.-L. Liu. 2011. The distribution of the ring current: Cluster observations. *Ann. Geo.* 29: 1655–1662. https://doi.org/10.5194/angeo-29-1655-2011.